Science and Technology Indonesia
e-ISSN:2580-4391 *p*-ISSN:2580-4405
Vol. 11, No. 1, January 2026

Research Paper

Structural, Electrochemical, Bacterial Activity, Hardness, and Thermal Properties of Mg Alloy with Various Zn Contents

Agung Premono[1*], Imam Basori[1], Ragil Sukarno[1], Ferry Budhi Susetyo[1], A. Ali Alhamidi[2], Hanif Setia Anugrah[1], Mochammad Fajr Dzakwan Muqafillah[1], Sigit Dwi Yudanto[3], Muhammad Yunan Hasbi[3], Evi Ulina Margareta Situmorang[4], Daniel Edbert[5], Etty Mutiara[6], Rosika Kriswarini[6], Agus Jamaludin[6], Maman Kartaman Ajiriyanto[6], Cahaya Rosyidan[7]

[1]*Department of Mechanical Engineering, Universitas Negeri Jakarta, Jakarta, 13220, Indonesia*
[2]*Department of Mechanical Engineering, Jenderal Sudirman University, Purwokerto, 53371, Indonesia*
[3]*Research Center for Metallurgy, National Research and Innovation Agency, Tangerang Selatan, Banten, 15314, Indonesia*
[4]*Department of Physiology School of Medicine and Health Sciences, Atma Jaya Catholic University of Indonesia, Jakarta, 14440, Indonesia*
[5]*Department of Microbiology, Atma Jaya Catholic University of Indonesia, Jakarta, 14440, Indonesia*
[6]*Research Center for Nuclear Material and Radioactive Waste Technology, National Research and Innovation Agency, Tangerang Selatan, Banten, 15314, Indonesia*
[7]*Department of Petroleum Engineering, Universitas Trisakti, Jakarta, 11440, Indonesia*
*__Corresponding author__: agung-premono@unj.ac.id

Abstract
Magnesium (Mg) alloy is used for various medical purposes, such as bone implants. In the present study, MgAlSixZn alloys were created utilizing the gravity casting by adding various Zinc (Zn) (x is 0, 0.5, 1.2, and 1.7 wt.%) and then homogenized at 400 °C for around two hours. MgAlSixZn as-homogenized samples were investigated for microstructure, phase structure, electrochemical behavior, surface morphology, bacterial activity, hardness, and thermal behavior using an optical microscope, XRD, Potentiostat, SEM-EDS, digital camera, Vickers hardness test, and Thermogravimetric apparatus, respectively. Several findings include that increasing Zn content implies a grain growth inhibition mechanism facilitated by Zn segregation at grain boundaries, increased corrosion rates, a rise in the hardness, and increased weight loss. It should be noted that the increase in the corrosion rate and weight loss occurs linearly for Zn addition in the Mg alloy until 1.2 wt.%. An increase in Zn concentration causes the peak shift in MgAlSi-based alloy samples, but no crystallographic orientation is apparent. At the end, the highest corrosion rate and inhibition area are observed in MgAlSi1.2Zn sample, which indicates that it is suitable for biodegradable orthopedic wire.

Keywords
Mg Alloy, Structure, EIS, *Staphylococcus aureus*, Vickers

Received: 19 July 2025, Accepted: 17 October 2025
https://doi.org/10.26554/sti.2026.11.1.96-108

1. INTRODUCTION

Magnesium (Mg) is becoming more and more popular in use due to its lightweight nature (Çiçek et al., 2013). Mg and its alloys are widely used in biomedical applications such as bone implants due to their good biocompatibility and degradability (Zhang et al., 2022). Bone implant materials are an essential component of biomedical materials, as around 70-80% of implants are made from biomedical alloys (Hafeez et al., 2019; Liu et al., 2020b). Unfortunately, some infections could occur due to bacterial agents. *Staphylococcus aureus* and *Staphylococcus epidermitis* are the most common causative agents (about 70%) of implant-associated infection in orthopedics (Wang et al., 2022).

There are a number of techniques to create an Mg alloy, such as powder metallurgy (Sharma et al., 2019), laser powder bed fusion additive manufacturing (Han et al., 2024), and casting using an electric furnace (Istrate et al., 2023) to improve the properties of the forming material. Several researchers have preferred to create Mg alloy using casting methods (Jiang et al., 2019; Nam, 2014; Singh et al., 2015). Besides using material fabrication techniques, some researchers doped other metals to achieve desired properties. The addition of Silicon (Si), Aluminum (Al), and Zinc (Zn) is a common metal added during the casting process. Wang et al. (2014b) found that an increase in the Si content in the MgAlSi alloy led to an increase in the tensile strength. Moreover, adding Al and Zn to the Mg alloy effectively strengthens the alloy (Li et al., 2022). Unfortunately, raising the Al and Zn can make the alloy easy to corrode (Candan and Candan, 2017; Song et al., 2012), but it could

also increase its hardness (Guo et al., 2017). However, presenting and increasing Zn content in the Mg alloy significantly improves antibacterial properties (He et al., 2015).

The considerable inhibition area and bacterial reduction in several investigations indicate that Zn in the alloy could enhance antibacterial properties (Bakhsheshi-Rad et al., 2017a,b). However, it also caused material degradation (crystal formation, holes, and hydrogen gas formation) and corrosion (Li et al., 2020; Liu et al., 2020a; Song et al., 2012; Zhao et al., 2016). Moreover, several reports of using Mg and Zn alloys have highlighted their stability and chemical stability (Wei et al., 2022; Zhang et al., 2022). However, it is reported that Mg is mainly biocompatible; integrating Mg into implants decreases mechanical stability due to the fast degradation of the material (Yu et al., 2018). Furthermore, using these materials as implants may be harmful due to oxidation processes, hole formation, and crystal deposition. These structural changes may affect mechanical integrity, especially in load-bearing applications, requiring adjustments to maintain antibacterial activity and guarantee durability. However, there is a potential for a biodegradable orthopedic wire (Cai et al., 2018; Han et al., 2024).

Several researchers create MgZn alloys using various combinations for different purposes. Yang et al. (2018), adding 1, 2, and 5 wt.% Mg to Zn to generate an effect galvanic cell. Ying et al. (2015) examine thermal conductivity as-cast and as-extruded MgxZn alloys (x is 0.5, 1, 1.5, 2.5, 4, and 5 wt.%) and found that increasing the Zn content leads to a decrease in thermal stability. Yan et al. (2017) investigating microstructure, mechanical properties, and corrosion behavior of MgxZn (x is 6, 14.5, 25.3, and 40.3 wt.%) as-extrude alloy. Cai et al. (2012) prepared Mg-Zn alloys with Zn contents of 1, 5, and 7 wt.% and investigated similar purposes to those of Yan et al. (2017). Jin et al. (2018) cast, extrude, and drew to diameter 0.25 mm of ZnxMg alloys (x is 0.08, 0.005, and 0.002 wt.%), then evaluated those as potential biodegradable stent materials. Guo et al. (2017) added Zn into AlMgSiCu alloys for automotive applications. Moreover, Zn, Mg, and Mg-Zn have different characteristics in inhibitive rate (Yu et al., 2017).

Various binary MgZn alloys have been widely investigated for physical, mechanical, electrochemical, and bacterial properties (Cai et al., 2012; Jin et al., 2018; Yan et al., 2017; Yang et al., 2018; Ying et al., 2015). According to several researchers' findings, testing for intermediate Zn concentrations (such as 0.5–1.7 wt.%) may create a balance between mechanical characteristics, material stability (corrosion), and antibacterial properties. Moreover, Guo et al. (2017) added Zn into AlMgSiCu alloys, and Jiao et al. (2021) added Zn into AlMgSi for automotive applications. To the best of our knowledge, no report has been conducted on MgAlSixZn alloy casting to investigate its microstructure, crystallographic orientation, electrochemical behavior, surface morphology, bacterial activity, hardness, and thermal characteristics. Therefore, the present study created MgAlSixZn using gravity casting by adding various amounts of Zn (x is 0, 0.5, 1.2, and 1.7 wt.%).

2. EXPERIMENTAL SECTION

2.1 Materials

MgAlSixZn was created by means of the gravity casting method by adding various Zn (x is 0, 0.5, 1.2, and 1.7 wt.%) (Guo et al., 2017; Li et al., 2018; Ying et al., 2015). Mg ingot was purchased from Fugu Yufeng Magnesium Co., Ltd, with a chemical composition of 99.92 wt.% Mg, 0.00163 wt.% Cu, 0.0167 wt. % Si, 0.0016 wt.% Fe, 0.0165 wt.% Mn, 0.00024 wt.% Ni and 0.0148 wt.% Al. A Zn ingot (99.996%) was purchased from Nyrstar, Australia, and the Al commercial used in the present study had a composition of 0.106 wt.% Si, 0.365 wt.% Fe, and Al balance.

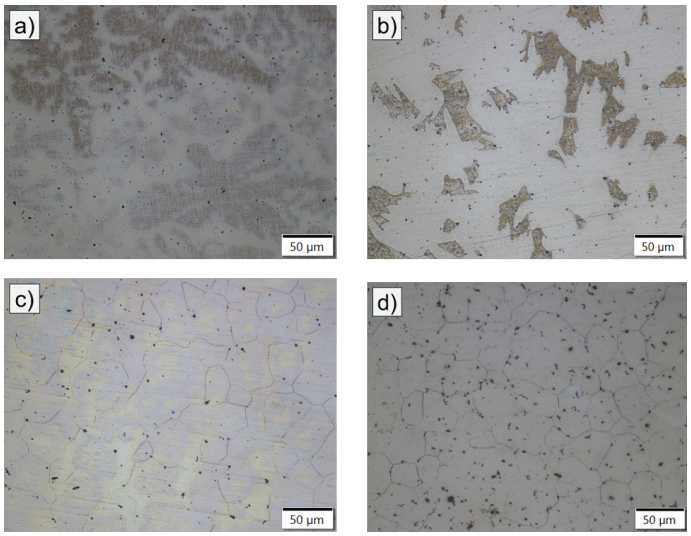

Figure 1. Microstructure of various samples (a) MgAlSi-0Zn, (b) MgAlSi-0.5Zn, (c) MgAlSi-1.2Zn, and (d) MgAlSi-1.7Zn

2.2 Instruments

A custom electric furnace was used to heat materials until they melted (Basori et al., 2025). After the specimens were created and homogenized, material characterization was performed. Various instruments were used in the present study for material characterization. X-ray fluorescence (XRF), Panalytical, Epsilon 4 type, was used to investigate the elements of the various samples. An optical microscope (Olympus BX53M) was used to capture the microstructure. The phase structure was investigated using X-ray diffraction (XRD) with a Bruker instrument. Hardness was measured using Vickers hardness equipment (FV-300e). The thermal behavior was studied using Thermogravimetry analysis (NETZSCH TG 209 F3 Tarsus). Electrochemical behavior was conducted using a Potentiostat (Gamry References 600). The surface morphology of the samples was also investigated using a scanning electron microscope (SEM) equipped with EDS (Thermo Scientific-Phenom Pharos). A sub-surface interaction test was documented using a camera (Samsung Galaxy S22) and a microscope (Olympus CX23).

2.3 Casting Process

Firstly, all ingot was inserted into the crucible and then followed by adding flux for around 3 wt.%. Flux was used as a composition of 55 wt.% KCl, 34 wt.% $MgCl_2$, 9 wt.% $BaCl_2$, and 2 wt.% CaF_2 (Merck with purity >99%) (Patel et al., 2021). After that, the crucible was heated using a custom electric furnace at 800 °C for around 15 minutes (Chakthin et al., 2016). After reaching the time, the melted ingot in the crucible was taken out, manually stirred, slag removed, and poured into a permanent mold (110×110×6 mm), accompanied by argon blow. Furthermore, the as-cast Mg alloys were homogenized at 400 °C for two hours (Wong et al., 2018).

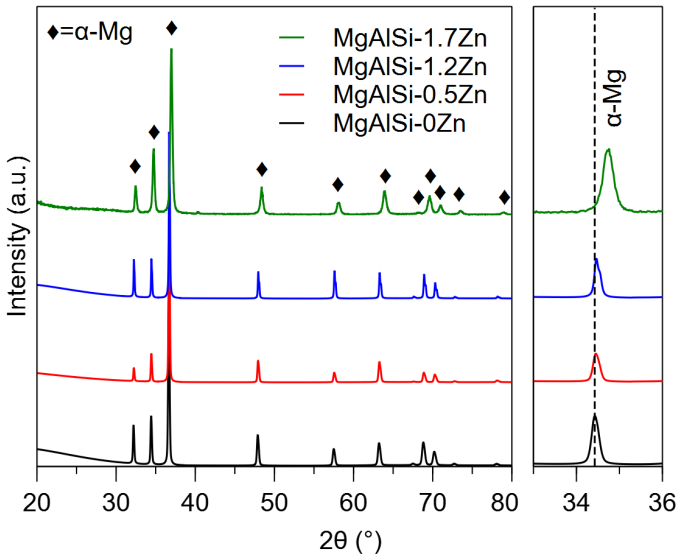

Figure 2. XRD Measurement Result. The Image on the Right Rhows the Magnified Diffraction Pattern at 2θ = 33 - 36°

2.4 Sample Preparation for Characterization

Mg alloys (as homogenized) were cut for several characterizations, such as XRF, microstructure, phase formation, electrochemical behavior, surface morphology, bacterial activity, hardness, and thermal analysis. Afterward, the samples were polished using silicon carbide (SiC) abrasive papers up to #3000, followed by aluminum oxide, until mirror polished, then etched using nital 2% for microstructure investigation (Syaripuddin et al., 2024). Samples for electrochemical behavior, surface morphology, bacterial activity, hardness, and thermal analysis were prepared similarly to the microstructure investigation (without etching).

2.5 Chemical Composition, Microstructure, Phase Structure, Hardness, and Thermal Behavior

The chemical composition of the as-homogenized Mg alloys was investigated using XRF. Microstructure was analyzed using an optical microscope. Phase structure was investigated using XRD, scanned from 20 to 80° using a step size of 0.020° (CuKα=1.5406 Å). The XRD data were refined using the General Structure Analysis System software (Larson and Von Dreele, 2004). Hardness was measured using Vickers hardness equipment. Five repeatable measurements were conducted using a 1kg load on different spots. Ultimately, thermal behavior was investigated using thermogravimetry analysis in a nitrogen environment (Basori et al., 2025).

2.6 Electrochemical Behavior

Electrochemical behavior was conducted using a Potentiostat on various samples with a surface area of 1 cm^2 (Syaripuddin et al., 2024). Three types of electrochemical behavior were investigated, including open circuit potential (OCP), potentiodynamic polarization (PP), and electrochemical impedance spectroscopy (EIS) in 0.9% NaCl at room temperature (Tasić et al., 2018). Prior to the PP measurement, OCP was scanned for 1200 seconds, and potential data was picked up every second. PP was conducted using a 1 mV/s scan rate (Syaripuddin et al., 2024)). In which Mg alloy is the working electrode, Platinum (Pt) is the counter electrode, and Ag/AgCl is the reference electrode. PP data was analyzed using the Tafel extrapolation method to determine corrosion current and potential. The corrosion rate is determined by inserting the corrosion current into Equation 1 (Ahmad, 2006).

$$Corrosion\ rate\ (mpy) = C.\frac{M_{icorr}}{n\rho} \quad (1)$$

Where ρ is alloy density (g/cm^3), icorr is corrosion current density (A/cm^2), M is atomic weight (g/mol), n is the number of electrons involved, and C is a constant (0.129 when corrosion rate is in mpy). Moreover, the EIS was conducted at 100000 to 0.2 Hz to find the Nyquist and Bode plots. Rct is charge transfer resistance, and Rs is solution resistance. Both were found by fitting using electrical equivalent circuits (EEC).

The surface morphology was investigated to compare the results of before-and-after corrosion tests. The surface morphology before the electrochemical test was captured by SEM. After the electrochemical test, the samples were also investigated using an SEM equipped with EDS. Moreover, the Image J software was used to analyze grain distribution diameters according to the SEM image after the electrochemical test (Rosyidan et al., 2024).

2.7 Bacterial Activity

The bacterial activity was conducted using *Staphylococcus aureus* ATCC 25923, employing the direct contact kill assay method, regrowth assessment, and the sub-surface interaction test. The direct contact kill assay method and regrowth assessment test are similar to those described in a previous study (Basori et al., 2025). Moreover, the last step in the bacterial activity is the sub-surface interaction test (pour plate modification) (Boczek et al., 2014). The cast metal was placed in the center, letting it be submerged within the liquid agar before it hardened. The whole system was then incubated at 37 °C and observed for 24

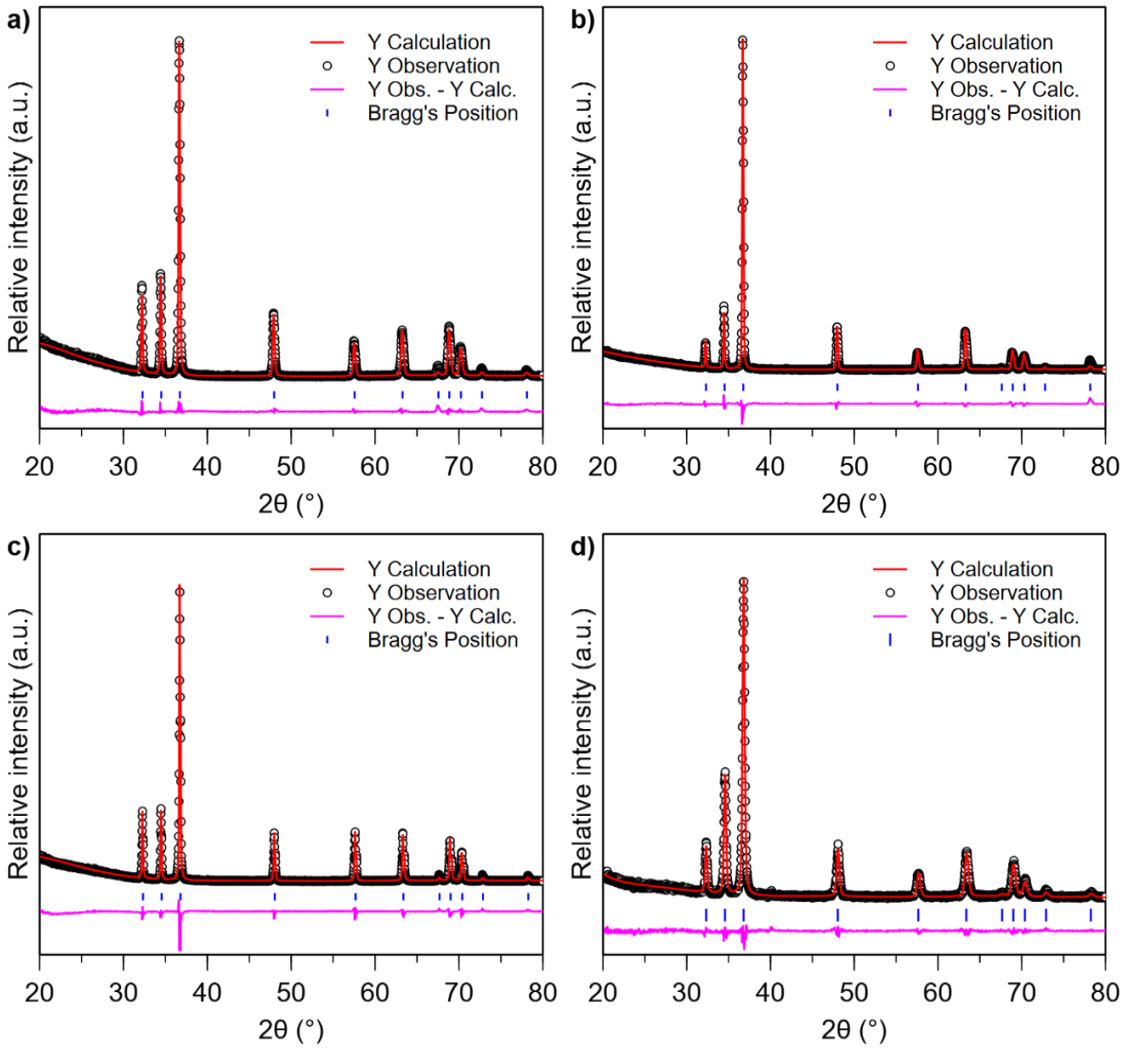

Figure 3. XRD Fitting Results (a) MgAlSi-0Zn, (b) MgAlSi-0.5Zn, (c) MgAlSi-1.2Zn, and (d) MgAlSi-1.7Zn

hours (captured with a camera). After incubation, the sample is picked up, and the agar is cut into transversal sections as thin as 0.5 mm with a sterile scalpel blade. The agar is put on a microscope slide and heat-fixed. The entire slide is flooded with Safranin 10%, water rinsed and then submerged in xylene: alcohol absolute 1:1 for 2 hours. It is then observed under 40× magnification on a microscope.

3. RESULTS AND DISCUSSION

3.1 Chemical Composition

The chemical, composition of the as-homogenized Mg alloys was investigated using XRF and presented in Table 1. Mg element is the majority offered in all alloy compositions. Although 0.060 wt.% Zn is present in the MgAlSi-0Zn; that sample was used as a Zn-free alloy. Moreover, comparing the chemical composition to AZ31B, AZ31, and AZ91D, it can be concluded chemical composition of the present study is not similar to the Mg standard alloys (Moreno et al., 2023; Setiawan and Rachman, 2021; Zaffora et al., 2021).

3.2 Microstructure

Figure 1 shows the microstructural evolution of the MgAlSixZn alloy as influenced by Zn addition. In the Zn-free alloy Figure 1a, the microstructure is dominated by coarse dendritic α-Mg structures, which indicate a relatively slow solidification rate and limited solute redistribution. Upon the addition of Zn Figure 1b, these dendrites transform into finer, more discrete secondary phase islands, suggesting a change in nucleation and growth behavior during solidification. Figures 1c and 1d reveal further grain refinement, as evidenced by the formation of well-defined grain boundaries across the matrix, with average grain sizes of 45 and 44.6 μm, respectively. The uniform appearance and absence of visible intermetallic phases suggest a homogeneous distribution of alloying elements and suppression of intermetallic compound formation under the applied processing conditions. The observed refinement with increas-

ing Zn content implies a grain growth inhibition mechanism facilitated by Zn segregation at grain boundaries. Accumulated Zn atoms at these boundaries hinder their mobility, thereby restricting grain coarsening during solidification or subsequent cooling (Yuan et al., 2022). This effect is commonly attributed to the solute drag phenomenon, in which segregated solute atoms exert a retarding force on moving grain boundaries, reducing their migration velocity and promoting finer grain structures (Guan et al., 2019).

Table 1. Chemical Composition of Various MgAlSiZn Alloys

Sample	Al	Si	Zn	Mg
		(wt. %)		
MgAlSi-0Zn	4.788	0.891	0.060	rest
MgAlSi-0.5Zn	5.314	0.315	0.531	rest
MgAlSi-1.2Zn	5.412	0.369	1.209	rest
MgAlSi-1.7Zn	0.641	0.523	1.739	rest

3.3 Phase Structure

Figure 2 shows the as-cast MgAlSi diffraction pattern with and without Zn addition. There are only diffraction peaks that can be identified as the α-Mg (pure Mg) phase in all four sample patterns. The hexagonal α-Mg phase peak with space group p63/mmc is in agreement with earlier studies (Guan et al., 2018; Hu et al., 2021; Wang et al., 2014a). In the results of the four samples, the β phase (Mg17Al12) was not detected. The peak shift in MgAlSi-based alloy samples is caused by an increase in Zn concentration, but no crystallographic orientation is apparent, as shown in Figure 2 (right image).

Figure 3 (a–d) shows a comparison of the calculated diffraction patterns with the observed results for the four samples. All four diffraction patterns were successfully calculated using the Rietveld method with the α-Mg phase as the reference. As the amount of Zn increases, the hexagonal crystals of the MgAlSi alloy become smaller. It is evident by the shrinkage in the lattice constant -c values, which decreases from 0.5196 nm to 0.5186 nm in the Zn-free sample and when Zn is added, respectively. The lattice constant -a value also decreased from 0.3201 nm to 0.3194 nm in comparison to the Zn-free sample when the Zn level rose to 1.2 wt.%. However, the sample with 1.7 wt.% Zn addition has almost identical lattice constant -a value as the sample with 1.2 wt.% Zn addition.

The Williamson-Hall plot method was used to determine how much Zn affects the mean crystallite size. In general, the Williamson-Hall method is a linear regression of the straight-line relationship between $\beta.\cos\theta$ and $4.\sin\theta$. The formula for this method is as follows in Equation 2 (Nath et al., 2020).

$$\beta \cos\theta = \frac{k\lambda}{D} + 4\epsilon \sin\theta \quad (2)$$

Where θ is the peak position (°), λ is the X-ray radiation wavelength (nm), ϵ is the micro-strain (%), β is the full width at half maximum (FWHM) value in radians, D is the mean crystallite size (nm), and k is the shape factor (k=0.94).

According to the calculations, adding Zn could refine the mean crystallite size. The sample containing 1.7 wt.% Zn had a mean crystallite size that was more than 3.5 times smaller than the Zn-free sample. Table 2 displays the mean crystallite size and the lattice parameter data from the calculation.

3.4 Electrochemical Behavior

Three types of electrochemical behavior were investigated, such as OCP, PP, and EIS in 0.9% NaCl at room temperature. OCP measurement results can be seen in Figure 4a. Generally, MgAlSi-1.2Zn and MgAlSi-1.7Zn have a stable potential at initial measurement until 1200 seconds, while MgAlSi-0Zn and MgAlSi-0.5Zn shift to more positive values. MgAlSi-0.5Zn and MgAlSi-0Zn at 400 and 600-second measurements suddenly move in a negative direction, which indicates the formation of $MgCl_2$ (Fitriana and Anawati, 2019). At the end of the OCP measurement, it was shown that decreasing the Zn content in the alloy led to shifting to more negative values of the samples. MgAlSi-0Zn has a more negative OCP value at 1200-second measurement, which indicates active behavior, probably due to Mg^{2+} ions that make the OCP value more negative (Singh et al., 2015).

The PP measurement was conducted after the OCP measurement, and the result is presented in Figure 4b. The Cathodic polarization curve is assumed to represent the hydrogen evolution reaction, as shown in the following reaction (Jiang et al., 2019).

$$2\,H_2O + 2\,e^- \longrightarrow 2\,OH^- + H_2\uparrow$$

The anodic curve dissolution represents the dissolution of Mg as follows (Jiang et al., 2019).

$$Mg \longrightarrow Mg^{2+} + 2\,e^-$$

The oxide layer of Mg mostly dissolves into solution when a chloride solution is exposed to a metal surface by releasing Mg ions to form $Mg(OH_2)$ (Saikrishna et al., 2016). $Mg(OH)_2$ is a little soluble and next reacts with Cl ions to form $MgCl_2$, and can also form complex Cl ions (Fitriana and Anawati, 2019).

Using Figure 4b, the Tafel extrapolation method was used to find corrosion current and potential. The corrosion rate can be found when a corrosion current is inserted into Equation 1. The Tafel extrapolation result and the corrosion rate are presented in Table 3. Increasing the Zn content in the alloy leads to an increase in corrosion rate. Saikrishna et al. state that the grain refinement influences the corrosion rate of the alloy (Saikrishna et al., 2016)). As shown in microstructure investigations, the Zn content increased to 0.5 wt.%, changing coarse dendritic transformations to finer ones. Moreover, Zn increased to 1.2 wt.% in the alloy, promoting a more refined grain. Those conditions result in a higher corrosion rate due to more Zn in the alloy, which implies a more refined grain. Interestingly, increasing the Zn content to 1.7 wt.% results in a decrease in corrosion rate. This behavior is due to the OCP measurement's slight shift to a more positive value, which indicates more corrosion resistance (Tasić et al., 2018).

Table 2. XRD Refinement Result

Source	MgAlSi-0Zn	MgAlSi-0.5Zn	MgAlSi-1.2Zn	MgAlSi-1.7Zn
Crystallographic data	Space group: p63/mmc (194) Crystal system: hexagonal Atomic coordinate: X=0.3333 Y=0.6667 Z=0.2500			
Lattice constants -**a** (nm)	0.3201	0.3197	0.3194	0.3195
Lattice constants -**c** (nm)	0.5196	0.5193	0.5188	0.5186
Mean crystallite size (nm)	482	362	145	132

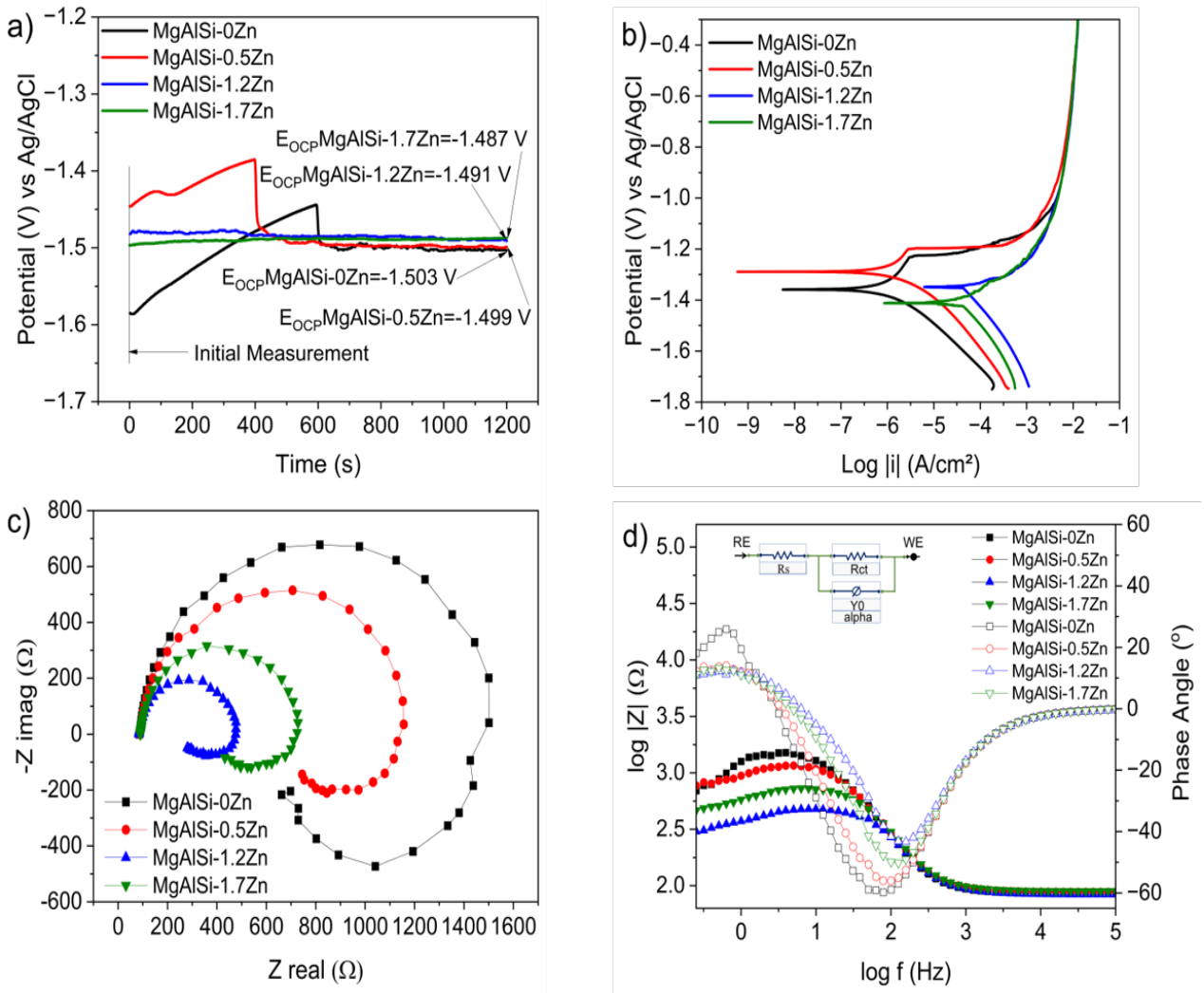

Figure 4. Electrochemical Behavior Result (a) OCP, (b) PP, (c) EIS-Nyquist Plot, and (d) EIS-Bode Plot

Furthermore, compared to another study, Mg has a more negative corrosion potential (-1.583 V vs. Ag/AgCl) than all the samples in the present study, and a higher corrosion current (56.9 μA/cm^2) than MgAlSi-0Zn and MgAlSi-0.5Zn samples in 0.9% NaCl solution (Ma et al., 2012).

Figure 4c presents the Nyquist plot of various samples. The highest capacitive arc is seen in MgAlSi-0Zn samples. Increased Zn content in the alloy linearly results in a decrease in the capacitive arc (except for 1.7 wt.% Zn). The highest capacitive arc indicates the sample has low metal dissolution,

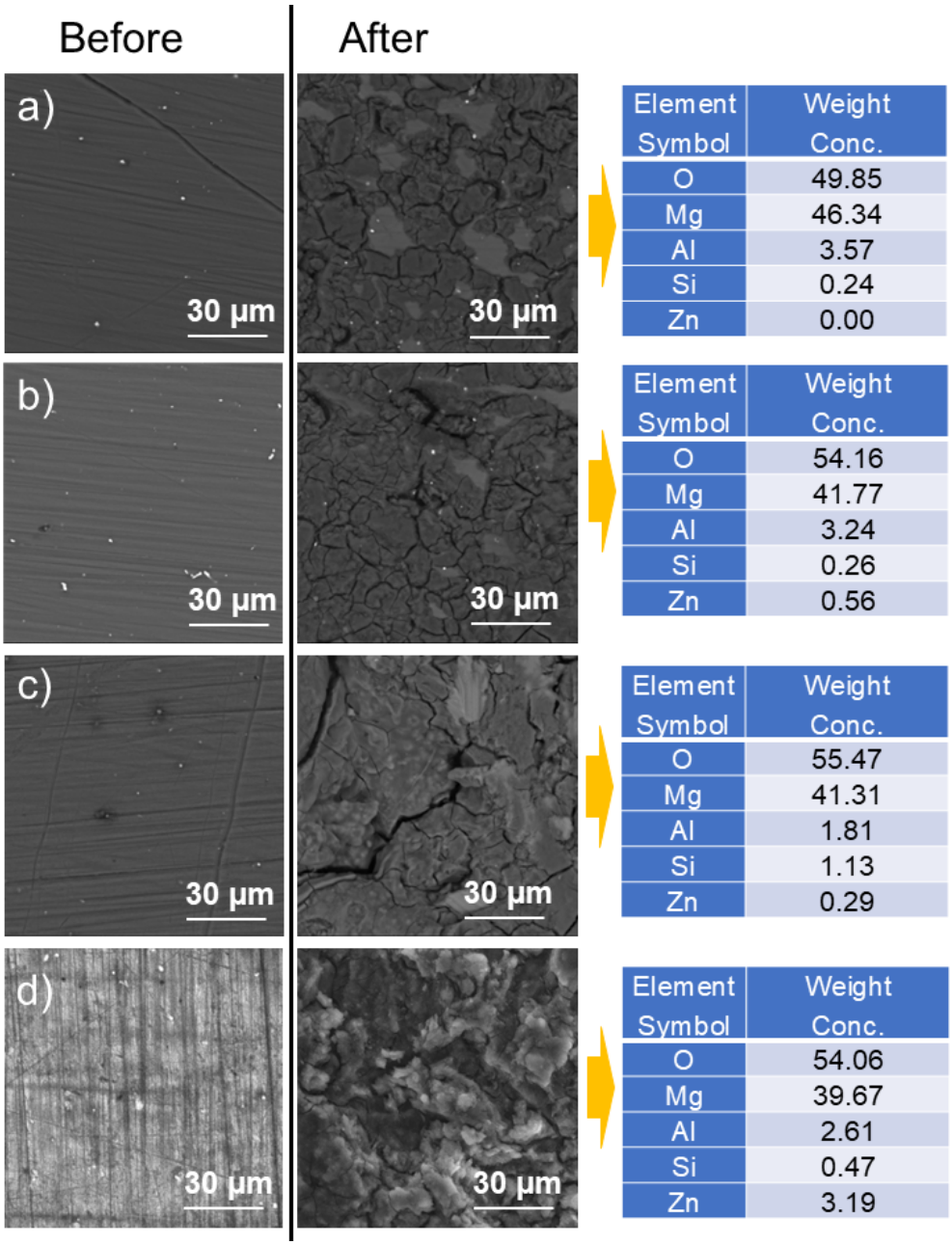

Figure 5. SEM Before and SEM-EDS After Electrochemical Measurement of Various Samples (a) MgAlSi-0Zn, (b) MgAlSi-0.5Zn, (c) MgAlSi-1.2Zn, and (d) MgAlSi-1.7Zn

while the lowest capacitive arc indicates higher metal dissolution. Moreover, the diameter of the arc is associated with the charge transfer resistance, which is related to the corrosion resistance of the samples in the solution (Oliveira et al., 2020). The MgAlSi-0Zn has a smaller diameter of the arc, which indicates that the surface of the sample formed a poor oxide that could not protect the alloy (Oliveira et al., 2014). Furthermore, an increase in the capacitive arc indicates that the oxide on top of the surface is more protective for the samples. This behavior is similar to the Song et al. (2012) study, in which varied Zn in the Mg.

Figure 4d presents a Bode plot of various samples that show the total impedance behavior. Phase maxima were shown at lower frequencies, which indicated the presence of the oxide film (Syaripuddin et al., 2024). The MgAlSi-1.2Zn sample presents the lowest phase maxima. Wang et al. (2023) have found that the lowest phase maxima could indicate the lowest corrosion resistance. Moreover, Rct is charge transfer resistance, and Rs is solution resistance. Both were found by fitting using electrical equivalent circuits (EEC), and the fitting results

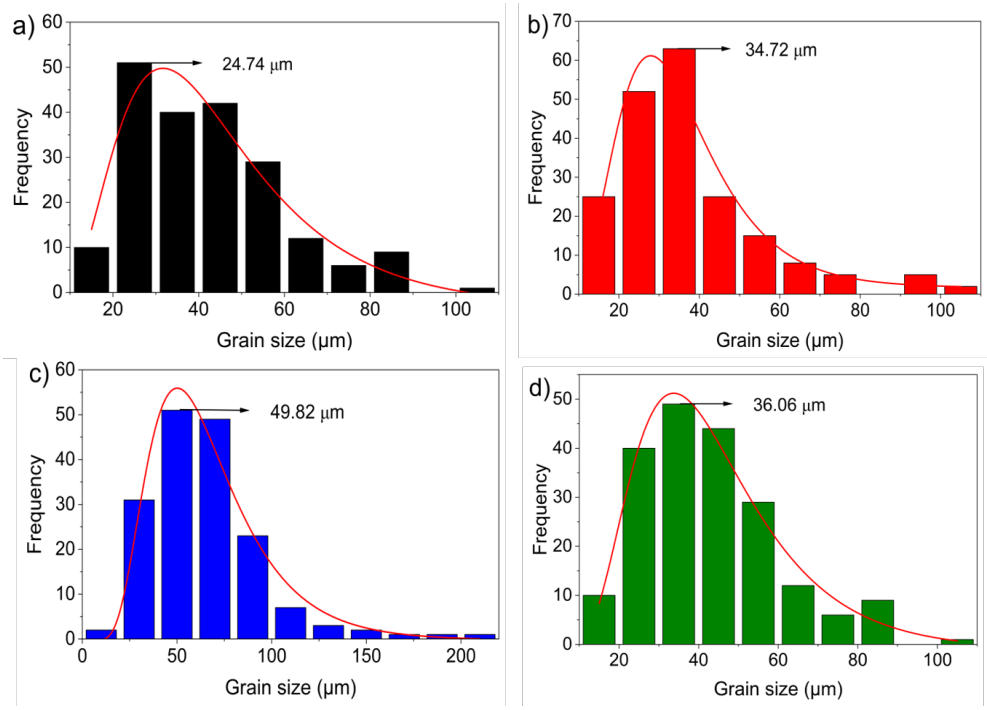

Figure 6. Grain Distribution According to the SEM Image After Electrochemical Measurement of Various Samples (a) MgAlSi-0Zn, (b) MgAlSi-0.5Zn, (c) MgAlSi-1.2Zn, and (d) MgAlSi-1.7Zn

Table 3. PP and EIS Investigation Result

Sample	PP			EIS	
	icorr ($\mu A/cm^2$)	Ecorr (V vs Ag/AgCl)	CR (mpy)	Rs (Ω)	Rct (Ω)
MgAlSi-0Zn	1.540	-1.359	2.79	85.74	1483
MgAlSi-0.5Zn	2.019	-1.289	3.65	88.54	1135
MgAlSi-1.2Zn	58.79	-1.349	106.30	84.53	389.1
MgAlSi-1.7Zn	50.32	-1.412	91.01	89.67	635.3

are shown in Table 3. The highest Rct indicates higher corrosion resistance Nam (2014), which is consistent with the PP result.

In order to get a better understanding of the electrochemical test sample's surface morphology, SEM was conducted before an electrochemical test and SEM-EDS after it Figure 5. Because of similar surface preparation, all samples had almost identical surface morphology before the test. Adding Zn in the alloy did not influence the surface morphology before the test. Compared to SEM before and after the electrochemical test, it can be seen that after the electrochemical test, the surface morphology experienced grain boundary corrosion. Corrosion would attack certain parts, such as holes or cracks (Kang et al., 2024). In the present study, an increase in Zn content up to 1.2 wt.% seems to have probably weakened grain boundary bonds. Therefore, the more Zn in the alloy, the more corrosion attacks are likely to occur at the grain boundary, indicating that MgAlSi-0Zn has better corrosion resistance. Furthermore, the grain distribution resulting from corrosion attack at the grain boundary was investigated and is presented in Figure 6. Increasing the Zn content up to 1.2 wt.% in the alloy leads to an increase in grain size. Moreover, in Figure 5, the phase can be seen on the sample's surfaces. After the electrochemical test exhibits the O phase, which indicates oxide on the surface of the samples (Saikrishna et al., 2016).

3.5 Bacterial Activity

The direct contact kill assay for 24 hours of incubation can be seen in Figure 7a. According to Image J software investigation, MgAlSi-0Zn, MgAlSi-0.5Zn, MgAlSi-1.2Zn, and MgAlSi-1.7Zn have inhibition areas of 0.11 ± 0.42, 0.03 ± 0.43, 2.27 ± 0.48, and 0.26 ± 0.55 cm^2, respectively. MgAlSi-1.2Zn samples showed the most significant inhibition area (2.27 ± 0.48 cm^2) and the diffusion of metallic ions into the agar. Besides

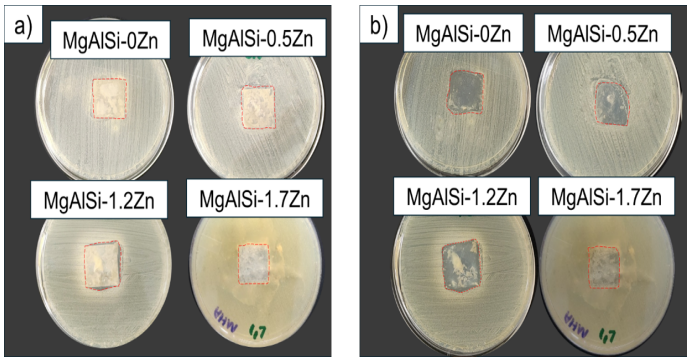

Figure 7. Bacterial Activity Documentation (a) Direct Contact Kill Assay After 24-Hours Incubation and (b) Regrowth Assessment After Removing the Mg Alloys for the Next 24 Hours

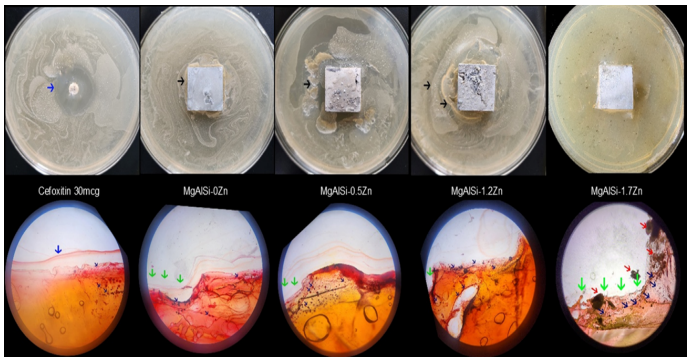

Figure 8. Sub-surface Interaction Test Result

Zn, Mg could also influence the inhibition area. Bakhsheshi-Rad et al. (2017b) have increased the Mg content in ZnAlMg alloy, resulting in an increase in the inhibition area from 1.9 ± 0.1 to 6.3 ± 0.2 mm.

The antibacterial action seems to be slow-acting, which is probably caused by the slow release of Zn ions, and the oxidation process of other materials. Extended antibacterial activity may be possible with this controlled release method. Through optimization of Zn concentration and release kinetics, the implant material could be modified to minimize degradation and sustain its antibacterial activity for a longer duration. Anodization or fluoride (F^-) coatings may assist in regulating Zn ion release without sacrificing antibacterial activity. Zn release can be slowed, fast oxidation can be avoided, and mechanical integrity can be enhanced by coating the implant with biodegradable polymers such as polylactic acid (PLA) or chitosan (Saberi et al., 2021; Tian and Liu, 2015). This difference in the antibacterial mechanism may suggest that MgAlSixZn antibacterial effects are caused by more than ion exchange or protein denaturation. Oxidative stress and the material's potential to be synergistic with human cells to combat infection and biofilm formation need to be further investigated.

Figure 7b shows the regrowth assessment after the removal of the Mg alloys for the next 24 hours. Crystal infiltrations are present inside the agar. The higher the Zn concentration, the larger the crystal. In general, the contact site remains sterile after the removal of the metal. The presence of crystal forms, possibly made of $MgSO_4$ and Al-based crystalline structures, demonstrated that higher Zn concentrations improved the transport of metallic ions (Zhang et al., 2020).

Mg corrosion products could inhibit the growth of *Staphylococcus aureus* (Bakhsheshi-Rad et al., 2017b). Moreover, Zn ions could be forming strong bonds of *Staphylococcus aureus* microorganism membranes protein (thiole, imidazole, amino, and carboxyl groups), inducing structural changes to membranes, hence disturbing protein transport and causing cell death (Zhao et al., 2016). Moreover, ROS generation could also inhibit the cell growth of the bacteria by destroying the cellular components (Bakhsheshi-Rad et al., 2017a).

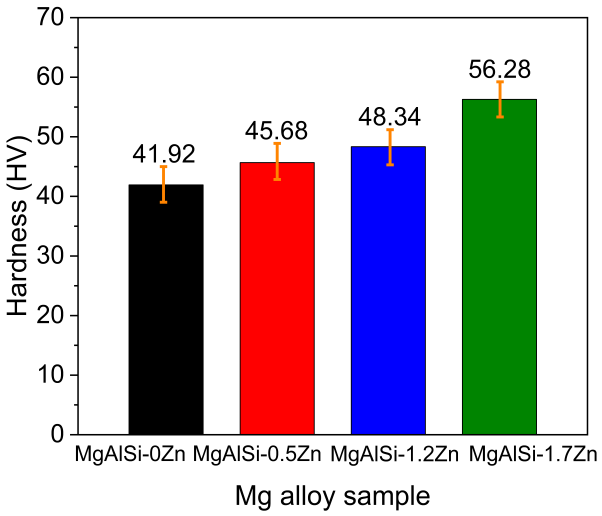

Figure 9. Average Hardness of Various Samples

The top pictures of Figure 8 show the condition of the sub-surface interaction test setting. Gas bubbles formed inside the agar (black arrow) and caused it to bulge and blow apart. This occurs especially in the materials that contain Zn (Liu et al., 2020a). Alloy materials containing Mg could also produce hydrogen gas (Yu et al., 2018). The bottom pictures of Figure 8 show transversal sections of agar stained with Safranin to depict the interaction between cast metal, a bacterial colony (small blue arrow, bottom pictures), and the agar. The blue arrow in the antibiotic picture indicates the inhibition area. The metal is placed while the agar is still liquid, resulting in the metal being submerged. No Inhibition area occurred around the samples compared to the control plate. Note that the bacterial colony still grew at the attachment site (green arrow). On the MgAlSi-1.2Zn sample, notice that a significant size of gas bubble formed inside the agar, numerous bacterial colonies grew inside it, and the bubble formation increases the surface area on which the bacteria could grow. On the MgAlSi-1.7Zn sample, Zn

deposits are embedded inside of the agar after sample removal (red Arrow).

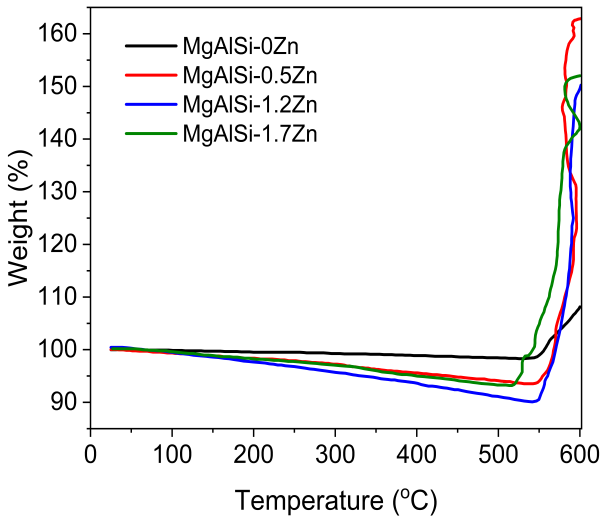

Figure 10. Thermal Behavior of Various Samples

3.6 Hardness

Hardness was measured using Vickers hardness equipment. Five repeatable measurements were conducted using 1kg of load. The average hardness of various Mg alloy samples can be found in Figure 9. Increasing the Zn content in the alloy increases the alloy's hardness. Jayalakshmi et al. (2014) found pure Mg has a hardness between 43 – 48 HV. Ramadhan and Zulfia (2020) found that the hardness of pure Mg is 39.67 HRH. The MgAlSi alloy (92.06 wt.% Mg, 7.82 wt.% Al, and 0.12 wt.% Si) has a hardness of 120 HV (Çiçek et al., 2013). Compared to the sample, MgAlSi-0Zn is different, probably due to the homogenize parameter being different (400 °C for 4 hours).

Increased Zn content in the alloy leads to an increase in hardness, which is similar to the Cai et al. (2012) study. Commonly, a smaller grain size could increase the hardness (Saikrishna et al., 2016). Besides grain sizes, crystallite size also influences the hardness of the alloys. The lowest crystallite size would result in higher hardness, which perfectly agrees with the present study (Senoz and Yilmaz, 2021).

3.7 Thermal behavior

Figure 10 shows the thermal behavior of various samples. The thermal behavior curve shows that it has two mechanisms. The first mechanism is decomposition for all samples until 518-545 °C, followed by the oxidation mechanism until 600 °C (Saraçoğlu et al., 2024; Zhang et al., 2023). Weight loss until 518-545 °C indicates degradation of the $Mg(OH)_2$ (Yu et al., 2016). While the oxidation mechanism until 600 °C would result in MgO, ZnO, and Al_2O_3, which could enhance the weight of the samples (Beder et al., 2024; Saraçoğlu et al., 2024). Moreover, presenting Zn content up to 1.2 wt.% in the alloy could increase the weight loss of the sample at 545 °C temperatures, which is in line with another study (Jones et al., 2013). On the contrary, Phetsinorath et al. (2012) found pure Mg would continuously increase the weight until 423 °C due to dehydriding.

4. CONCLUSIONS

MgAlSixZn (x is 0, 0.5, 1.2, and 1.7 wt.%) were produced using gravity casting and have been well created and analyzed. Increasing Zn content implies a mechanism for grain growth inhibition, facilitated by Zn segregation at grain boundaries, reduction of crystallite size, decrease in capacitive arc, and increased weight loss. It should be noted that the reduction of the capacitive arc and the increased weight loss occur for Zn addition in the alloy until 1.2 wt.%. Reduction in crystallite size is promoting an increase in hardness. While the decrease in capacitive arc indicates that the sample is easily corroded, corrosion resistance is reduced. Furthermore, the highest corrosion rate and inhibition area are observed in MgAlSi1.2Zn sample, which suggests that it is suitable for biodegradable orthopedic wire. Recommendations for future work include testing in biological fluids and long-term degradation studies. In vivo studies also should assess the host tissue response, cytotoxicity, and osseointegration of the Zn-modified MgAlSi alloy.

5. ACKNOWLEDGMENT

Universitas Negeri Jakarta funded this research with Contract Number 30/KN/LPPM/III/2025 (12 March 2025).

REFERENCES

Ahmad, Z. (2006). *Principles of Corrosion Engineering and Corrosion Control*. Elsevier

Bakhsheshi-Rad, H., E. Hamzah, A. Ismail, M. Aziz, M. Kasiri-Asgarani, E. Akbari, S. Jabbarzare, A. Najafinezhad, and Z. Hadisi (2017a). Synthesis of a Novel Nanostructured Zinc Oxide/baghdadite Coating on Mg Alloy for Biomedical Application: In-Vitro Degradation Behavior and Antibacterial Activities. *Ceramics International*, **43**(17); 14842–14850

Bakhsheshi-Rad, H., E. Hamzah, H. Low, M. Kasiri-Asgarani, S. Farahany, E. Akbari, and M. Cho (2017b). Fabrication of Biodegradable Zn-Al-Mg Alloy: Mechanical Properties, Corrosion Behavior, Cytotoxicity and Antibacterial Activities. *Materials Science and Engineering: C*, **73**; 215–219

Basori, I., Y. Sari, D. W. Prasetya, F. B. Susetyo, J. U. Alias, S. Budi, S. D. Yudanto, M. Hasbi, E. U. M. Situmorang, and D. Edbert (2025). A Small Amount of Sn Addition Effect to Cu-15Zn Alloy on Structure, Microstructure, Hardness, Corrosion Resistance, and Antibacterial Activity. *Science and Technology Indonesia*, **10**(2); 443–451

Beder, M., S. B. Akçay, T. Varol, and H. Çuvalcı (2024). The Effect of Heat Treatment on the Mechanical Properties and Oxidation Resistance of Alsi10mg Alloy. *Arabian Journal for Science and Engineering*, **49**(11); 15335–15346

Boczek, L. A., E. W. Rice, and C. H. Johnson (2014). Pour Plate Technique. In *Encyclopedia of Food Microbiology*, volume 3. Academic Press, London, pages 625–629

Cai, H., Y. Zhang, X. Li, J. Meng, F. Xue, C. Chu, L. Tao, and J. Bai (2018). Self-Reinforced Biodegradable Mg-2Zn Alloy Wires/Polylactic Acid Composite for Orthopedic Implants. *Composites Science and Technology*, **162**; 198–205

Cai, S., T. Lei, N. Li, and F. Feng (2012). Effects of Zn on Microstructure, Mechanical Properties and Corrosion Behavior of Mg-Zn Alloys. *Materials Science and Engineering: C*, **32**(8); 2570–2577

Candan, S. and E. Candan (2017). A Comparative Study on Corrosion of Mg-Al-Si Alloys. *Transactions of Nonferrous Metals Society of China*, **27**(8); 1725–1734

Chakthin, S., P. Kahawong, and P. Senthongkaew (2016). The Modification of β-Al5FeSi Phase in Al-Si-Mg-Fe Alloys by Utilizing Recycled Beverage Can Body in Casting Process. *Key Engineering Materials*, **675**; 660–663

Çiçek, B., H. Ahlatçı, and Y. Sun (2013). Wear Behaviours of Pb Added Mg-Al-Si Composites Reinforced with in Situ Mg2si Particles. *Materials & Design*, **50**; 929–935

Fitriana, M. and A. Anawati (2019). Remarkable Improvement in Corrosion Resistance of Anodized AZ31 Alloy by Sealing with Beeswax-Colophony Resin. In *Journal of Physics: Conference Series*, volume 1191. IOP Publishing, page 012032

Guan, D., X. Liu, J. Gao, L. Ma, B. P. Wynne, and W. M. Rainforth (2019). Exploring the Mechanism of "Rare Earth" Texture Evolution in a Lean Mg-Zn-Ca Alloy. *Scientific Reports*, **9**(1); 7152

Guan, M., Y. Hu, T. Zheng, T. Zhao, and F. Pan (2018). Composition Optimization and Mechanical Properties of Mg-Al-Sn-Mn Alloys by Orthogonal Design. *Materials*, **11**(8); 1424

Guo, M., X. Zhang, J. Zhang, and L. Zhuang (2017). Effect of Zn Addition on the Precipitation Behaviors of Al-Mg-Si-Cu Alloys for Automotive Applications. *Journal of Materials Science*, **52**(3); 1390–1404

Hafeez, N., S. Liu, E. Lu, L. Wang, R. Liu, L.-C. Zhang, and W. Lu (2019). Mechanical Behavior and Phase Transformation of β-Type Ti-35Nb-2Ta-3Zr Alloy Fabricated by 3D-Printing. *Journal of Alloys and Compounds*, **790**; 117–126

Han, C., J. Huang, X. Ye, B. Liu, Z. Dong, Y. Yang, J. Gao, K. Yang, and G. Chen (2024). Microstructure Evolution and Ductility Improvement of Additively Manufactured Biodegradable Zinc-Magnesium Alloys Via Annealing. *International Journal of Bioprinting*, **10**(4); 3034

He, G., Y. Wu, Y. Zhang, Y. Zhu, Y. Liu, N. Li, M. Li, G. Zheng, B. He, Q. Yin, Y. Zheng, and C. Mao (2015). Addition of Zn to the Ternary Mg-Ca-Sr Alloys Significantly Improves Their Antibacterial Properties. *Journal of Materials Chemistry B*, **3**(32); 6676–6689

Hu, C., C. Chen, and M. Zhang (2021). Effects of Ag Content and Heat Treatment on the Microstructure and Properties of SLMed AZ61 Mg-Al-Zn Alloy. *Applied Physics A*, **127**(3); 186

Istrate, B., C. Munteanu, M.-S. Bălțatu, R. Cimpoeșu, and N. Ioanid (2023). Microstructural and Electrochemical Influence of Zn in MgCaZn Biodegradable Alloys. *Materials*, **16**(6); 2487

Jayalakshmi, S., S. Sahu, S. Sankaranarayanan, S. Gupta, and M. Gupta (2014). Development of Novel Mg-Ni60Nb40 Amorphous Particle Reinforced Composites with Enhanced Hardness and Compressive Response. *Materials and Design*, **53**; 849–855

Jiang, P., C. Blawert, R. Hou, N. Scharnagl, J. Bohlen, and M. L. Zheludkevich (2019). Microstructural Influence on Corrosion Behavior of MgZnGe Alloy in NaCl Solution. *Journal of Alloys and Compounds*, **783**; 179–192

Jiao, N., Y. Lai, S. Chen, P. Gao, and J. Chen (2021). Atomic-Scale Roles of Zn Element in Age-Hardened AlMgSiZn Alloys. *Journal of Materials Science dan Technology*, **70**; 105–112

Jin, H., S. Zhao, R. Guillory, P. K. Bowen, Z. Yin, A. Griebel, J. Schaffer, E. J. Earley, J. Goldman, and J. W. Drelich (2018). Novel High-Strength, Low-Alloys Zn-Mg (< 0.1 Wt% Mg) and Their Arterial Biodegradation. *Materials Science and Engineering: C*, **84**; 67–79

Jones, F., H. Tran, D. Lindberg, L. Zhao, and M. Hupa (2013). Thermal Stability of Zinc Compounds. *Energy and Fuels*, **27**(10); 5663–5669

Kang, Y.-x., Z.-l. Li, S.-f. Yan, W.-d. Chen, and C.-x. Guo (2024). Optimization of Anodizing Conditions and Hole Sealing Treatments for Enhanced Anti-Corrosion Properties of Magnesium Alloys. *Ceramics International*, **50**(14); 25667–25678

Larson, A. C. and R. B. Von Dreele (2004). General Structure Analysis System (GSAS). Technical report, Los Alamos

Li, J., Y. Bian, X. Tu, W. Li, and D. Song (2022). Influence of Surface Roughness of Substrate on Corrosion Behavior of MAO Coated ZM5 Mg Alloy. *Journal of Electroanalytical Chemistry*, **910**; 116206

Li, L., S. Ji, Q. Zhu, Y. Wang, X. Dong, W. Yang, S. Midson, and Y. Kang (2018). Effect of Zn Concentration on the Microstructure and Mechanical Properties of Al-Mg-Si-Zn Alloys Processed by Gravity Die Casting. *Metallurgical and Materials Transactions A*, **49**(8); 3247–3256

Li, Y., C. Liao, and S. C. Tjong (2020). Recent Advances in Zinc Oxide Nanostructures with Antimicrobial Activities. *International Journal of Molecular Sciences*, **21**(22); 8836

Liu, D., Q. Gao, Q. An, H. Wang, J. Wei, and C. Wei (2020a). Experimental Study on Zn-Doped Al-Rich Alloys for Fast On-Board Hydrogen Production. *Crystals*, **10**(3); 167

Liu, S., J. Liu, L. Wang, R. L.-W. Ma, Y. Zhong, W. Lu, and L.-C. Zhang (2020b). Superelastic Behavior of In-Situ Eutectic-Reaction Manufactured High Strength 3D Porous Niti-Nb Scaffold. *Scripta Materialia*, **181**; 121–126

Ma, N., Q. Peng, X. Li, H. Li, J. Zhang, and Y. Tian (2012). Influence of Scandium on Corrosion Properties and Electrochemical Behaviour of Mg Alloys in Different Media. *International Journal of Electrochemical Science*, **7**(9); 8020–

8034
Moreno, J., J. L. Merlo, A. C. Renno, J. Canizo, F. J. Buchelly, J. I. Pastore, M. R. Katunar, and S. Cere (2023). In Vitro Characterization of Anodized Magnesium Alloy As a Potential Biodegradable Material for Biomedical Applications. *Electrochimica Acta*, **437**; 141463
Nam, N. D. (2014). Corrosion Behavior of Mg–5Al Based Magnesium Alloy with 1 Wt.% Sn, Mn and Zn Additions in 3.5 Wt.% NaCl Solution. *Journal of Magnesium and Alloys*, **2**(2); 190–195
Nath, D., F. Singh, and R. Das (2020). X-Ray Diffraction Analysis by Williamson-Hall, Halder-Wagner and Size-Strain Plot Methods of CdSe Nanoparticles-A Comparative Study. *Materials Chemistry and Physics*, **239**; 122021
Oliveira, L. A. d., R. M. P. da Silva, A. C. D. Rodas, R. M. Souto, and R. A. Antunes (2020). Surface Chemistry, Film Morphology, Local Electrochemical Behavior and Cytotoxic Response of Anodized AZ31B Magnesium Alloy. *Journal of Materials Research and Technology*, **9**(6); 14754–14770
Oliveira, M. C. L. D., V. S. M. Pereira, O. V. Correa, and R. A. Antunes (2014). Corrosion Performance of Anodized AZ91D Magnesium Alloy: Effect of the Anodizing Potential on the Film Structure and Corrosion Behavior. *Journal of Materials Engineering and Performance*, **23**(2); 593–603
Patel, S. M., M. M. Patel, and V. J. Rao (2021). Synthesis and Characterization of Magnesium Melting Fluxes. *Materials Research Express*, **8**(11); 116503
Phetsinorath, S., J.-x. Zhou, X.-x. Zeng, H.-q. Sun, and W.-j. Ding (2012). Preparation and Hydrogen Storage Properties of Ultrafine Pure Mg and Mg-Ti Particles. *Transactions of Nonferrous Metals Society of China*, **22**(8); 1849–1854
Ramadhan, R. and A. Zulfia (2020). Study on the Effect of Volume Fraction (Vf%) SiC Addition to the Characteristics of Mg-Al-Sr/SiC Composites Using Stir Casting Method. In *IOP Conference Series: Materials Science and Engineering*, volume 924. IOP Publishing, page 012022
Rosyidan, C., B. Kurniawan, B. Soegijono, M. Maulani, L. Samura, F. G. Nababan, V. G. V. Putra, and F. B. Susetyo (2024). Nickel Salt Dependency as Catalyst in the Plating Bath on the Film Properties of Cu/Cu-Ni. *Science and Technology Indonesia*, **9**(3); 529–538
Saberi, A., H. R. Bakhsheshi-Rad, S. Abazari, A. F. Ismail, S. Sharif, S. Ramakrishna, M. Daroonparvar, and F. Berto (2021). A Comprehensive Review on Surface Modifications of Coatings Opportunities and Challenges. *Coatings*, **11**(7); 747
Saikrishna, N., G. Pradeep Kumar Reddy, B. Munirathinam, and B. Ratna Sunil (2016). Influence of Bimodal Grain Size Distribution on the Corrosion Behavior of Friction Stir Processed Biodegradable AZ31 Magnesium Alloy. *Journal of Magnesium and Alloys*, **4**(1); 68–76
Saraçoğlu, T. N., S. Polat, E. Koç, M. Mashra, A. N. Saud, and M. Michalska-Domańska (2024). Investigating the Oxidation Behavior of Mg-Zn Alloy: Effects of Heating Rates, Gas Flow, Protective Atmosphere, and Alloy Composition. *Journal of Metals, Materials and Minerals*, **34**(3); 1–11
Senoz, G. M. L. and T. A. Yilmaz (2021). Optimization of Equal Channel Angular Pressing Parameters for Improving the Hardness and Microstructure Properties of Al-Zn-Mg Alloy by Using Taguchi Method. *Metals and Materials International*, **27**(3); 436–448
Setiawan, A. R. and M. D. Rachman (2021). An Investigation of Pulse Anodization Duty Ratio and Sealing Treatment on the Corrosion Behavior of the Anodic Coating Layer in Magnesium AZ31B. *Corrosion Science and Technology*, **20**(2); 45–51
Sharma, N., G. Singh, P. Sharma, and A. Singla (2019). Development of Mg-Alloy by Powder Metallurgy Method and Its Characterization. *Powder Metallurgy and Metal Ceramics*, **58**(3-4); 163–169
Singh, I. B., M. Singh, and S. Das (2015). A Comparative Corrosion Behavior of Mg, AZ31 and AZ91 Alloys in 3.5% NaCl Solution. *Journal of Magnesium and Alloys*, **3**(2); 142–148
Song, Y., E. H. Han, D. Shan, C. D. Yim, and B. S. You (2012). The Effect of Zn Concentration on the Corrosion Behavior of Mg-xZn Alloys. *Corrosion Science*, **65**; 322–330
Syaripuddin, S., M. F. P. Putra, M. K. Ajiriyanto, S. D. Yudanto, M. Y. Hasbi, and F. B. Susetyo (2024). Nichrome Dependency in Welding Layer Using In situ Fabrication on Hardness and Corrosion Properties. *Science and Technology Indonesia*, **9**(3); 651–659
Tasić, Z. Z., M. B. Petrović Mihajlović, M. B. Radovanović, and M. M. Antonijević (2018). Electrochemical Investigations of Copper Corrosion Inhibition by Azithromycin in 0.9% NaCl. *Journal of Molecular Liquids*, **265**; 687–692
Tian, P. and X. Liu (2015). Surface Modification of Biodegradable Magnesium and Its Alloys for Biomedical Applications. *Regenerative Biomaterials*, **2**(2); 135–151
Wang, N., Y. Ma, H. Shi, Y. Song, S. Guo, and S. Yang (2022). Mg-, Zn-, and Fe-Based Alloys With Antibacterial Properties as Orthopedic Implant Materials. *Frontiers in Bioengineering and Biotechnology*, **10**; 859341
Wang, N., R. Wang, C. Peng, B. Peng, Y. Feng, and C. Hu (2014a). Discharge Behaviour of Mg-Al-Pb and Mg-Al-Pb-In Alloys as Anodes for Mg-Air Battery. *Electrochimica Acta*, **149**; 193–205
Wang, X., Y. Tao, X. Yang, Y. Deng, D. Zhu, D. Dong, and T. Ma (2023). Enhanced Corrosion Resistance and Hardness of CoCrCuFeNi Alloy Under High-Pressure Solidification. *Intermetallics*, **154**; 107778
Wang, Y., H. Liao, Y. Wu, and J. Yang (2014b). Effect of Si Content on Microstructure and Mechanical Properties of Al-Si-Mg Alloys. *Materials and Design*, **53**; 634–638
Wei, Y., J. Wang, S. Wu, R. Zhou, K. Zhang, Z. Zhang, J. Liu, S. Qin, and J. Shi (2022). Nanomaterial-Based Zinc Ion Interference Therapy to Combat Bacterial Infections. *Frontiers in Immunology*, **13**; 884766
Wong, T. W., A. Hadadzadeh, M. J. Benoit, and M. A. Wells (2018). Impact of Homogenization Heat Treatment on the

High Temperature Deformation Behavior of Cast AZ31B Magnesium Alloy. *Journal of Materials Processing Technology*, **254**; 238–247

Yan, Y., H. Cao, Y. Kang, K. Yu, T. Xiao, J. Luo, Y. Deng, H. Fang, H. Xiong, and Y. Dai (2017). Effects of Zn Concentration and Heat Treatment on the Microstructure, Mechanical Properties and Corrosion Behavior of As-Extruded Mg-Zn Alloys Produced by Powder Metallurgy. *Journal of Alloys and Compounds*, **693**; 1277–1289

Yang, H., X. Qu, W. Lin, D. Chen, D. Zhu, K. Dai, and Y. Zheng (2018). Enhanced Osseointegration of Zn-Mg Composites by Tuning the Release of Zn Ions with Sacrificial Mg-Rich Anode Design. *ACS Biomaterials Science and Engineering*, **5**(2); 453–467

Ying, T., M. Y. Zheng, Z. T. Li, X. G. Qiao, and S. W. Xu (2015). Thermal Conductivity of As-Cast and As-Extruded Binary Mg-Zn Alloys. *Journal of Alloys and Compounds*, **621**; 250–255

Yu, X., B. Jiang, J. He, B. Liu, Z. Jiang, and F. Pan (2016). Effect of Zn Addition on the Oxidation Property of Mg-Y Alloy at High Temperatures. *Journal of Alloys and Compounds*, **687**; 252–262

Yu, Y., G. Jin, Y. Xue, D. Wang, X. Liu, and J. Sun (2017). Multifunctions of Dual Zn/Mg Ion Co-implanted Titanium on Osteogenesis, Angiogenesis and Bacteria Inhibition for Dental Implants. *Acta Biomaterialia*, **49**; 590–603

Yu, Y., H. Lu, and J. Sun (2018). Long-Term In Vivo Evolution of High-Purity Mg Screw Degradation-Local and Systemic Effects of Mg Degradation Products. *Acta Biomaterialia*, **71**; 215–224

Yuan, M., C. He, Y. Song, B. Lei, X. Qian, Z. Dong, J. Zhao, H. Yang, Y. Chai, B. Jiang, and F. Pan (2022). Effects of Zn Addition on the Microstructure and Mechanical Properties of As-Extruded Mg-2Al-0.5Ca Alloy. *Metals*, **12**(2); 221

Zaffora, A., F. Di Franco, D. Virtù, F. Carfì Pavia, G. Ghersi, S. Virtanen, and M. Santamaria (2021). Tuning of the Mg Alloy AZ31 Anodizing Process for Biodegradable Implants. *ACS Applied Materials and Interfaces*, **13**(11); 12866–12876

Zhang, C., J. Lin, N. Y. T. Nguyen, Y. Guo, C. Xu, C. Seo, E. Villafana, H. Jimenez, Y. Chai, R. Guan, and H. Liu (2020). Antimicrobial Bioresorbable Mg-Zn-Ca Alloy for Bone Repair in a Comparison Study With Mg-Zn-Sr Alloy and Pure Mg. *ACS Biomaterials Science and Engineering*, **6**(1); 517–538

Zhang, M. X., C. G. Zhu, X. Xie, and S. Y. Liu (2023). Kinetics and Combustion Behavior of Atomized Zn-Mg Alloy Powder. *ACS Omega*, **8**(27); 24503–24512

Zhang, T., W. Wang, J. Liu, L. Wang, Y. Tang, and K. Wang (2022). A Review on Magnesium Alloys for Biomedical Applications. *Frontiers in Bioengineering and Biotechnology*, **10**; 1004738

Zhao, C., H. Wu, P. Hou, J. Ni, P. Han, and X. Zhang (2016). Enhanced Corrosion Resistance and Antibacterial Property of Zn Doped DCPD Coating on Biodegradable Mg. *Materials Letters*, **180**; 42–46

